J. Fluid Mech. (2025), *vol.* 1012, R2, doi:10.1017/jfm.2025.10173



A unified framework for mean temperature analysis in compressible turbulent channel flows

Xuke Zhu[1], **Peng Zhang**[2], **Xiaoshuo Yang**[1], **Yongchao Ji**[1] **and Zhenhua Xia**[1]

[1]State Key Laboratory of Fluid Power and Mechatronic Systems and Department of Engineering Mechanics, Zhejiang University, Hangzhou 310027, PR China

[2]College of Metrology and Measurement Engineering, China Jiliang University, Hangzhou 310018, PR China

Corresponding author: Zhenhua Xia, xiazh1006@163.com

(Received 2 January 2025; revised 22 April 2025; accepted 23 April 2025)

We present a unified framework derived from the total heat flux equation, enabling the direct formulation of the relationship between mean temperature and velocity fields, as well as the development of mean temperature scalings in compressible turbulent channel flows. The proposed mean temperature–velocity relationship, combined with a simple damping function model for the mixed Prandtl number, demonstrates high efficacy in channels with both symmetric and asymmetric thermal boundary conditions across a range of Mach and Reynolds numbers. In contrast, the state-of-the-art generalised Reynolds analogy (GRA) relation (Zhang *et al.*, 2014, *J. Fluid Mech.*, vol. 739, pp. 392–420) is shown to be insufficient for asymmetric cases due to mismatched boundary conditions at the effective boundary layer edge. By introducing a mean temperature decomposition, we clarify that while the GRA relation effectively characterises the component associated with turbulence production and viscous dissipation, it fails to account for the contribution arising from non-zero edge total heat flux. Furthermore, we rigorously derive mean temperature transformations compatible with arbitrary velocity scalings for the first time. These findings provide some physical insights into the mean momentum and heat transport in compressible wall-bounded turbulence, and may be helpful for developing near-wall models.

Key words: compressible turbulence, turbulence theory

1. Introduction

The interplay between momentum and heat transfer in compressible wall-bounded turbulence has received significant attention due to its crucial role in advancing reduced-order modelling and improving predictions of aerodynamic forces and heating

© The Author(s), 2025. Published by Cambridge University Press.

https://doi.org/10.1017/jfm.2025.10173 Published online by Cambridge University Press

(Cheng *et al.* 2024; Yu *et al.* 2024). Significant efforts have been devoted to establishing connections between mean velocity and temperature fields, with existing approaches broadly divided into two categories.

The first category relies on the intrinsic similarity between velocity and temperature fields, commonly referred to as the Reynolds analogy. The first recognised expression for compressible turbulent boundary layer flows (CTBLFs) with $Pr = 1$ (where Pr denotes the molecular Prandtl number) was derived by Busemann (1931) and Crocco (1932), by adopting the strong similarity assumption. It was later extended to cases with $Pr \neq 1$ by introducing a recovery factor $r \approx Pr^{1/3}$, known as Walz's equation (Walz 1969), which, however, is limited to flows with adiabatic walls. Based on direct numerical simulations (DNS) data of CTBLFs, Duan & Martin (2011) proposed an empirical formula that improves on Walz's equation, independent of Mach number, wall temperature, surface catalysis and enthalpy conditions. Recently, Zhang *et al.* (2014) introduced a generalised recovery factor r_g to account for diabatic walls, and developed the generalised Reynolds analogy (GRA) theory. The resulting mean temperature–velocity relationship is given as

$$\frac{\tilde{T}}{\tilde{T}_w} = 1 + \frac{\tilde{T}_{rg} - \tilde{T}_w}{\tilde{T}_w}\frac{\tilde{u}}{\tilde{u}_e} + \frac{\tilde{T}_e - \tilde{T}_{rg}}{\tilde{T}_w}\left(\frac{\tilde{u}}{\tilde{u}_e}\right)^2, \tag{1.1}$$

where $\tilde{T}_{rg} = \tilde{T}_e + r_g\tilde{u}_e^2/(2c_p)$ with $r_g = 2c_p(\tilde{T}_w - \tilde{T}_e)/\tilde{u}_e^2 + 2c_p/\tilde{u}_e \times \partial\tilde{T}/\partial\tilde{u}|_w$, and c_p denotes the specific heat capacity at constant pressure. Here, the subscripts w and e denote values at the wall and the effective boundary layer edge (Lusher & Coleman 2022; Huang *et al.* 2023), respectively. It has been demonstrated that (1.1) is fundamentally equivalent to Duan's empirical formula and remains effective across a wide range of canonical flows, making it the most advanced model to date. A recent work by Cheng & Fu (2024*b*) further extended the framework of the GRA theory, enhancing the depiction of fluctuating fields while confirming that (1.1) continues to be a robust approximation for mean fields. Most recently, Chen, Gan & Fu (2025) systematically re-evaluated the performance of the GRA relations in both laminar and turbulent channel and boundary layer flows. They demonstrated that the generalised recovery factor r_g is not constant but exhibits at least moderate wall-normal variations in most cases. Through sensitivity analysis based on the effective Prandtl number Pr_e, they elucidated the success of the GRA relations in compressible turbulent channel flows (CTCFs) and CTBLFs as well as the deviations observed in laminar boundary layers. Furthermore, they refined the GRA relations by proposing a more general wall-normal distribution of the effective Prandtl number, rather than simply assuming a constant value $Pr_e \equiv 1$ (Zhang *et al.* 2014).

Building on the success of mean velocity scalings (Van Driest 1951; Trettel & Larsson 2016; Griffin, Fu & Moin 2021; Hasan *et al.* 2023; Zhu *et al.* 2024), the second category attempts to find a mapping that transforms compressible mean temperature profiles to their 'incompressible' counterparts. The pioneering work appears to stem from Patel, Boersma & Pecnik (2017), where the authors developed two types of mean temperature transformations for turbulent channel flows with variable properties at low Mach numbers. Chen *et al.* (2022*a*) later extended them to high-speed flows by additionally incorporating viscous heating, resulting in the Van Driest (VD)-type and Trettel–Larsson (TL)-type transformations applicable to both isothermal and adiabatic walls. Huang *et al.* (2023) further discarded the higher-order terms and derived closed-form expressions for the two transformations mentioned above in CTCFs, leveraging the similarity between the mean transport equations and their 'incompressible' counterparts. Most recently, Cheng & Fu (2024*a*) clarified the impact of these approximations and proposed a novel Mach number

https://doi.org/10.1017/jfm.2025.10173 Published online by Cambridge University Press

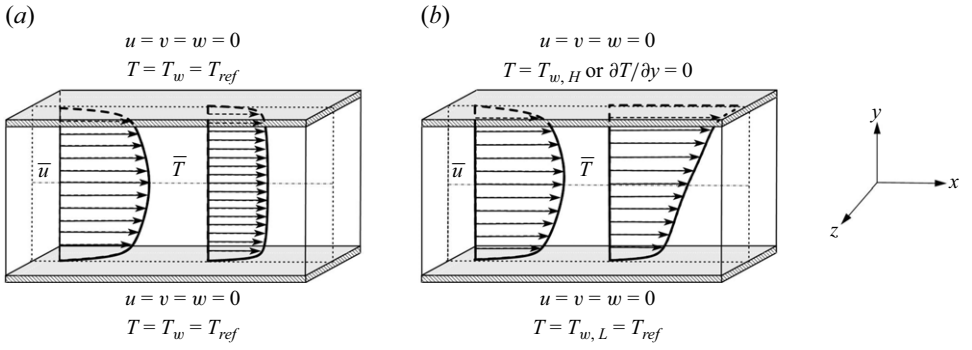


Figure 1. Illustrations of CTCFs with (*a*) symmetric and (*b*) asymmetric thermal boundary conditions.

independent scaling, whose integration leads to a transformation that outperforms the TL-type transformation in CTCFs with adiabatic walls and in CTBLFs with cold walls.

In this paper, a unified framework for mean temperature analysis based on the total heat flux equation is proposed in CTCFs, which allows for the direct derivation of mean temperature–velocity relations without relying on similarity assumptions, and facilitates the development of more advanced mean temperature transformations.

2. Derivation of the general framework

We focus on fully developed CTCFs with both symmetric and asymmetric thermal boundary conditions. The flow is driven by the streamwise body force F and governed by the compressible Navier–Stokes equations

$$\begin{aligned} \frac{\partial \rho}{\partial t} + \frac{\partial \rho u_j}{\partial x_j} &= 0, \\ \frac{\partial \rho u_i}{\partial t} + \frac{\partial \rho u_i u_j}{\partial x_j} &= -\frac{\partial p}{\partial x_i} + \frac{\partial \tau_{ij}}{\partial x_j} + F\delta_{i1}, \\ \frac{\partial \rho E}{\partial t} + \frac{\partial \left[u_j\,(\rho E + p)\right]}{\partial x_j} &= \frac{\partial u_i \tau_{ij}}{\partial x_j} - \frac{\partial q_j}{\partial x_j} + F u_1, \end{aligned} \tag{2.1}$$

with the viscous stress τ_{ij} and molecular heat flux q_j given as

$$\tau_{ij} = \mu\left(\frac{\partial u_i}{\partial x_j} + \frac{\partial u_j}{\partial x_i} - \frac{2}{3}\frac{\partial u_k}{\partial x_k}\delta_{ij}\right), \quad q_j = -\lambda\frac{\partial T}{\partial x_j}. \tag{2.2}$$

Here, δ_{ij} denotes the Kronecker delta, and $i = 1, 2, 3$ represent the streamwise (x), wall-normal (y) and spanwise (z) directions, respectively. The fluid is considered as a calorically perfect gas, characterised by the equation of state $p = \rho R T$, where p, ρ, R and T denote the pressure, density, specific gas constant and temperature, respectively. Also, u_i is the ith velocity component, and $E = e + u_i u_i/2$ is the total energy per unit mass, where $e = c_v T$ is the internal energy, with $c_v = R/(\gamma - 1)$ being the specific heat capacity at constant volume, and $\gamma = c_p/c_v = 1.4$ the specific heat ratio. The dynamic viscosity μ follows Sutherland's law or the power law $\mu \propto T^{0.7}$ (Lusher & Coleman 2022), and the thermal conductivity is given by $\lambda = \mu c_p/Pr$, with a constant Prandtl number.

As shown in figure 1, periodic boundary conditions are applied in the streamwise and spanwise directions, while no-slip conditions are imposed for velocity at the walls. In the symmetric case, both walls are maintained at the same temperature T_w (Yao & Hussain 2020; Zhang & Xia 2020; Zhang, Song & Xia 2023). In the asymmetric

https://doi.org/10.1017/jfm.2025.10173 Published online by Cambridge University Press

case, the lower wall is fixed at $T_{w,L}$, while the upper wall is either adiabatic ($\partial T/\partial y = 0$) (Lusher & Coleman 2022) or fixed at $T_{w,H}$ (Zhang, Song & Xia 2024). In the following, both Reynolds averaging $\phi = \bar{\phi} + \phi'$ and Favre averaging $\phi = \tilde{\phi} + \phi''$ are employed to decompose the quantity ϕ into its mean and fluctuating components. The friction velocity $u_\tau = \sqrt{\bar{\tau}_w/\bar{\rho}_w}$ (where $\bar{\tau}_w = \bar{\tau}_{12}|_w$ is the wall shear stress) and the viscous length scale $\delta_v = \bar{\mu}_w/(\bar{\rho}_w u_\tau)$ characterise the inner scaling with a superscript +, while the semi-local friction velocity $u_\tau^* = \sqrt{\bar{\tau}_w/\bar{\rho}}$ and viscous length scale $\delta_v^* = \bar{\mu}/(\bar{\rho}u_\tau^*)$ define the semi-local scaling with a superscript $*$.

The integral of the Reynolds-averaged momentum and total energy equations in (2.1) reveals the balance between molecular and turbulent diffusion fluxes (Huang, Coleman & Bradshaw 1995):

$$\bar{\mu}\,\frac{\mathrm{d}\tilde{u}}{\mathrm{d}y} - \bar{\rho}\,\widetilde{u''v''} \approx \bar{\tau}_w - \int_0^y \bar{F}\,\mathrm{d}y \tag{2.3}$$

and

$$\bar{\mu}\,\frac{\mathrm{d}\tilde{K}}{\mathrm{d}y} - \bar{\rho}\,\widetilde{K''v''} + \bar{\mu}\,\frac{\mathrm{d}\tilde{k}}{\mathrm{d}y} - \bar{\rho}\,\widetilde{k''v''} + \bar{\lambda}\,\frac{\mathrm{d}\tilde{T}}{\mathrm{d}y} - c_p\bar{\rho}\,\widetilde{T''v''} \approx -\bar{q}_w - \int_0^y \overline{Fu}\,\mathrm{d}y. \tag{2.4}$$

Here, $\bar{\tau}_t = \bar{\mu}\,\mathrm{d}\tilde{u}/\mathrm{d}y - \bar{\rho}\,\widetilde{u''v''}$ is the total shear stress, and $\bar{q}_w = \bar{q}_2|_w$ is the wall heat flux. The decomposition of the instantaneous kinetic energy, $u_i u_i/2 = \tilde{K} + K'' + \tilde{k} + k''$, is introduced to simplify $\overline{\tau_{i2}u_i}$, where $\tilde{K} = \tilde{u}_i\tilde{u}_i/2$, $K'' = \tilde{u}_i u_i''$, $\tilde{k} = \widetilde{u_i''u_i''}/2$ and $k'' = u_i''u_i''/2 - \widetilde{u_i''u_i''}/2$ (Huang *et al.* 1995, 2023). Additionally, the molecular diffusion flux of a quantity ϕ, $\overline{\mu\,\mathrm{d}\phi/\mathrm{d}y}$, is approximated by its dominant term $\bar{\mu}\,\mathrm{d}\tilde{\phi}/\mathrm{d}y$ during the above derivation.

Following previous studies (Zhang *et al.* 2014; Huang *et al.* 2023; Cheng & Fu 2024*a*), the quasi-parallel flow approximation $u_i u_i \approx u^2$ and small turbulence approximation $u^2 \approx \tilde{u}^2 + 2\tilde{u}u''$ are further adopted. These approximations are intended to exclude higher-order terms, commonly absent in open-source DNS data, thereby preserving the simplicity of turbulence modelling. However, they do introduce some non-negligible effects on accuracy, such as $\overline{\tau_{i2}u_i} \approx \bar{\mu}\tilde{u}\,\mathrm{d}\tilde{u}/\mathrm{d}y$ near the adiabatic wall, as detailed by Cheng & Fu (2024*a*) and in Appendix A. Anyway, the total heat flux equation can then be derived by combining (2.3) and (2.4) while assuming $\overline{Fu} = \bar{F}\tilde{u}$:

$$\bar{q}_t = -\left(\bar{\lambda} + \bar{\lambda}_t\right)\frac{\mathrm{d}\tilde{T}}{\mathrm{d}y} = \bar{q}_w + \int_0^y \bar{\tau}_{12}\frac{\mathrm{d}\tilde{u}}{\mathrm{d}y}\,\mathrm{d}y + \int_0^y \bar{R}_{12}\frac{\mathrm{d}\tilde{u}}{\mathrm{d}y}\,\mathrm{d}y, \tag{2.5a}$$

$$\bar{q}_t = -\left(\bar{\lambda} + \bar{\lambda}_t\right)\frac{\mathrm{d}\tilde{T}}{\mathrm{d}y} = \bar{q}_{t,e} - \int_y^{\delta_e} \bar{\tau}_{12}\frac{\mathrm{d}\tilde{u}}{\mathrm{d}y}\,\mathrm{d}y - \int_y^{\delta_e} \bar{R}_{12}\frac{\mathrm{d}\tilde{u}}{\mathrm{d}y}\,\mathrm{d}y. \tag{2.5b}$$

It is important to note that (2.5*a*) and (2.5*b*) represent the forms integrated from the wall ($y = 0$) and the effective boundary layer edge ($y = \delta_e$, where $\mathrm{d}\tilde{u}/\mathrm{d}y = 0$), respectively. Here, $\bar{\lambda}_t = -c_p\bar{\rho}\,\widetilde{T''v''}/(\mathrm{d}\tilde{T}/\mathrm{d}y)$ is the eddy thermal conductivity, $\bar{\tau}_{12} = \bar{\mu}\,\mathrm{d}\tilde{u}/\mathrm{d}y$ is the mean viscous shear stress, and $\bar{R}_{12} = -\bar{\rho}\,\widetilde{u''v''}$ is the turbulent shear stress. Additionally, $\bar{q}_{t,e} = (-\bar{\lambda}\,\mathrm{d}\tilde{T}/\mathrm{d}y + c_p\bar{\rho}\,\widetilde{T''v''})|_e$ denotes the mean total heat flux at the effective boundary layer edge $y = \delta_e$. The physical significance is clear: for instance, (2.5*a*) indicates that the difference between the total heat flux $\bar{q}_t(y)$ and wall heat flux $\bar{q}_w$ arises from the production of turbulent kinetic energy and molecular viscous dissipation within the control volume $[0, y]$. Notably, unlike previous approaches (Chen *et al.* 2022*a*;

https://doi.org/10.1017/jfm.2025.10173 Published online by Cambridge University Press

Huang *et al.* 2023; Cheng & Fu 2024*a*), the constant-stress layer approximation $\bar{\tau}_t \approx \bar{\tau}_w$ has not been applied directly.

Inspired by the derivation of Walz's equation (Walz 1969; Smits & Dussauge 2006; Zhang *et al.* 2014), we introduce the eddy viscosity $\bar{\mu}_t = -\bar{\rho}\,\widetilde{u''v''}/(\mathrm{d}\tilde{u}/\mathrm{d}y)$ and the mixed Prandtl number $Pr_m = c_p(\bar{\mu}+\bar{\mu}_t)/(\bar{\lambda}+\bar{\lambda}_t)$, while acknowledging that $\tilde{T} = \tilde{T}(\tilde{u})$. Subsequently, $\bar{\rho}_w c_p u_\tau \tilde{T}_w$ is divided out from both sides of (2.5*a*) and (2.5*b*), leading to their dimensionless forms as

$$\frac{\bar{\tau}_t^+}{Pr_m}\frac{\mathrm{d}\theta}{\mathrm{d}\tilde{u}^+} = B_q + (\gamma-1)\,M_\tau^2\int_0^{\tilde{u}^+}\bar{\tau}_t^+\,\mathrm{d}\tilde{u}^+, \quad \theta|_w = 0, \tag{2.6a}$$

$$\frac{\bar{\tau}_t^+}{Pr_m}\frac{\mathrm{d}\theta}{\mathrm{d}\tilde{u}^+} = Q_{t,e} - (\gamma-1)\,M_\tau^2\int_{\tilde{u}^+}^{\tilde{u}_e^+}\bar{\tau}_t^+\,\mathrm{d}\tilde{u}^+, \quad \theta|_w = 0, \tag{2.6b}$$

where $B_q = \bar{q}_w/(\bar{\rho}_w c_p u_\tau \tilde{T}_w)$ is the dimensionless wall heat flux, $M_\tau = u_\tau/\sqrt{\gamma R\tilde{T}_w}$ is the friction Mach number, $Q_{t,e} = \bar{q}_{t,e}/(\bar{\rho}_w c_p u_\tau \tilde{T}_w)$ is the dimensionless total heat flux at the effective boundary layer edge, and $\tilde{u}_e$ is the mean velocity at the effective boundary layer edge. The dimensionless mean temperature $\theta = 1-\tilde{T}/\tilde{T}_w$ can be determined directly by integrating (2.6*a*), provided that B_q, M_τ, $\bar{\tau}_t^+$, $\tilde{u}^+$, Pr_m are known:

$$\begin{gathered}\theta(B_q, M_\tau, \bar{\tau}_t^+, \tilde{u}^+, Pr_m) = \int_0^{\tilde{u}^+}\frac{Pr_m}{\bar{\tau}_t^+}f(B_q, M_\tau, \bar{\tau}_t^+, \tilde{u}^+)\,\mathrm{d}\tilde{u}^+,\\ f(B_q, M_\tau, \bar{\tau}_t^+, \tilde{u}^+) = B_q + (\gamma-1)M_\tau^2\int_0^{\tilde{u}^+}\bar{\tau}_t^+\,\mathrm{d}\tilde{u}^+.\end{gathered} \tag{2.7}$$

In the constant-stress layer of high Reynolds number flows, where $y/\delta_e \ll 1$, the approximation $\bar{\tau}_t^+ \approx 1$ is typically adopted, simplifying (2.7) to

$$\theta(B_q, M_\tau, \tilde{u}^+, Pr_m) = \int_0^{\tilde{u}^+} Pr_m\left[B_q + (\gamma-1)\,M_\tau^2\tilde{u}^+\right]\mathrm{d}\tilde{u}^+. \tag{2.8}$$

If $Pr_m \approx Pr$ is further adopted in the near-wall region ($y^* \lesssim 5$), then a quadratic relationship between the mean temperature and mean velocity can be given as (Huang & Coleman 1994)

$$\theta(B_q, M_\tau, \tilde{u}^+, Pr) = Pr\,B_q\tilde{u}^+ + (\gamma-1)\,M_\tau^2\frac{Pr}{2}\tilde{u}^{+2}. \tag{2.9}$$

In CTCFs, $\bar{\tau}_t^+$ can be derived theoretically from the mean streamwise momentum equation. Consequently, (2.7)–(2.9) can be interpreted as the mean temperature–velocity relation and its two approximations, when Pr_m is appropriately modelled. The two key wall parameters, B_q and M_τ, make them potentially applicable across a wide range of wall thermodynamic conditions and Mach numbers. Additionally, it is worth noting that the mean temperature–velocity relation derived by Huang, Bradshaw & Coakley (1993), Huang & Coleman (1994) and Huang *et al.* (2023) can be regarded as a special case of (2.8) in the logarithmic layer, where $Pr_m \approx Pr_t \approx \kappa/\kappa_T \approx 0.85$.

3. The modelling of Pr_m

Drawing on the DNS data from Abe & Antonia (2019) and Lluesma-Rodríguez *et al.* (2018), Huang *et al.* (2023) demonstrated that $Pr_m(y^+)$ (Pr_{total} in their paper) exhibits an excellent collapse at $y^+ \lesssim 10$, attains peak value approximately 1 at $y^+ \approx 50$, and

https://doi.org/10.1017/jfm.2025.10173 Published online by Cambridge University Press

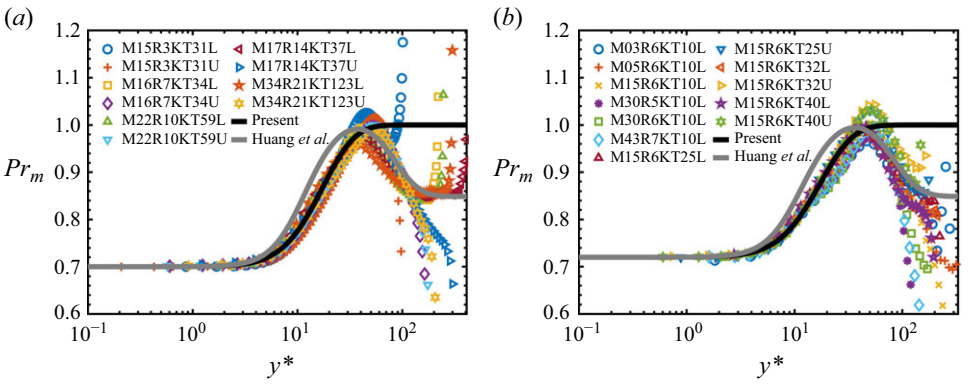


Figure 2. Comparison of the performance of (3.1) (black solid lines) with Huang's model (grey solid lines) for modelling $Pr_m(y^*)$, in both symmetric and asymmetric CTCFs, with (*a*) $Pr = 0.7$ (Lusher & Coleman 2022) and (*b*) $Pr = 0.72$ (Zhang & Xia 2020; Zhang *et al.* 2023, 2024). The definitions of the labels are provided in § 4.

levels off at 0.85 for $y^+ \gtrsim 150$ in flows with $Re_\tau > 1000$. Meanwhile, a similar trend was observed in the semi-local coordinate y^* using the compressible DNS data provided by Lusher & Coleman (2022). Consequently, they extended the incompressible Pr_m model to compressible flows by assuming the Mach independence of $Pr_m(y^*)$. Nonetheless, in order to minimise the number of empirical parameters while maintaining simplicity, we prefer employing a damping function to directly capture the universal profile of $Pr_m(y^*)$ before its peak, i.e.

$$Pr_m(y^*) = Pr + (1 - Pr)\, D^*_{Pr_m}, \quad D^*_{Pr_m}(y^*) = \left[1 - \exp\left(-y^*/A^*_{Pr_m}\right)\right]^n. \tag{3.1}$$

The empirical parameters $A^*_{Pr_m} = 10$ and $n = 3$ are obtained by fitting the DNS data from Lusher & Coleman (2022), including the $Pr_m(y^*)$ profiles on both the isothermal cold wall and adiabatic hot wall sides at $y^* \leqslant 50$. The present model is thoroughly compared with both DNS data and the model proposed by Huang *et al.* (2023), as shown in figure 2. It is apparent that our model shows significant improvement before the peak, which dominates the accuracy of (2.7). While Huang's model remains effective post-peak, we have decided to abandon such modelling. The implications and justification for this simplification will be discussed in the next section and Appendix A.

Additionally, special attention should be given to the fact that the proposed model implies $Pr_m - Pr = \mathcal{O}(y^{*3})$ as $y^* \to 0$, which does not align with the asymptotic behaviour at the wall under various thermal boundary conditions. For instance, in incompressible wall-bounded turbulence with constant properties, asymptotic analysis reveals that while the proposed model satisfies the imposed temperature boundary condition, it fails to account for adiabatic and imposed heat flux conditions. Although not shown here, this discrepancy can be observed for $y^* \lesssim 3$ when using a log-log scale instead of a semi-logarithmic scale. Undoubtedly, a more accurate, physics-informed model would be preferable, necessitating a detailed investigation of the behaviour of Pr_m both near the wall and beyond its peak. The current model serves as a temporary compromise, and future studies are expected to further refine and improve it.

4. Verification and evaluation

In this section, DNS data of CTCFs are employed to systematically evaluate the mean temperature–velocity relation derived from the GRA theory, as given in (1.1), where $\tilde{T}_e$

https://doi.org/10.1017/jfm.2025.10173 Published online by Cambridge University Press

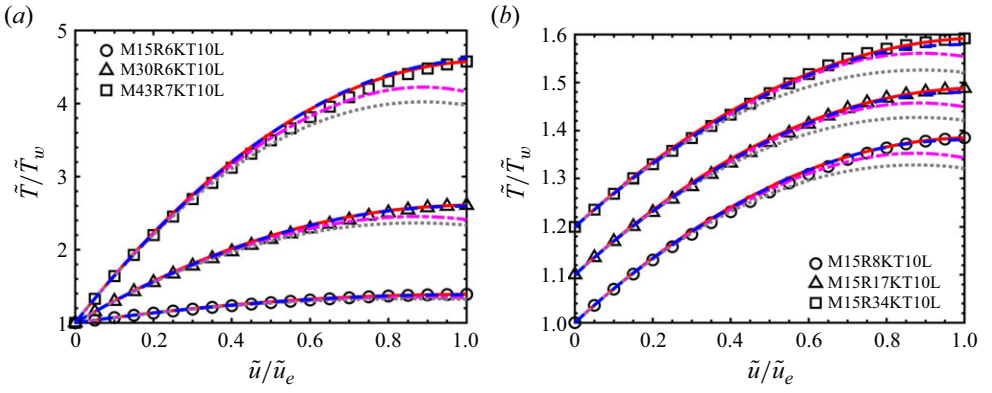


Figure 3. Comparison of DNS data for symmetric cases (symbols) with various mean temperature-velocity relations: (1.1) (red solid lines), (2.7) (blue dashed lines), (2.8) (pink dash-dotted lines) and (2.9) (grey dotted lines). The datasets are sourced from (*a*) Zhang & Xia (2020) and Zhang *et al.* (2023), and (*b*) Yao & Hussain (2020). For clarity, the results in (*b*) are shifted upwards.

is obtained from the DNS data, alongside the proposed relations in (2.7)–(2.9), with Pr_m determined by (3.1). The dataset encompasses symmetric cases with isothermal walls from Yao & Hussain (2020), Zhang & Xia (2020) and Zhang *et al.* (2023), as well as those with asymmetric thermal boundary conditions from Lusher & Coleman (2022) and Zhang *et al.* (2024). For clarity, all cases are relabelled in this paper. For instance, 'M15R6KT32L(H)' refers to the flow region near the lower cold (upper hot) wall, with bulk Mach number $M_b = 1.5$, bulk Reynolds number $Re_b = 6000$, and wall temperature ratio between the upper hot and lower cold wall of $\tilde{T}_{w,H} \approx 3.2\tilde{T}_{w,L} = 3.2T_{ref}$.

In channels with symmetric isothermal walls, the total shear stress is $\bar{\tau}_t^+ = 1 - y/h$ when the flow is driven by a uniform body force. To derive $\tilde{T}/\tilde{T}_w = 1 - \theta$ via (2.7), B_q, M_τ, $\tilde{u}^+$, y/h, y^* and Pr are required. Figure 3 provides a comprehensive comparison of the proposed mean temperature–velocity relation and its approximations (2.7)–(2.9), alongside the GRA relation (1.1). As observed, the GRA relation and the proposed one demonstrate nearly equivalent performance, with the former showing a slight advantage as $\tilde{u}/\tilde{u}_e \to 1$ due to $\tilde{T}_e$ being directly constrained by DNS data. The constant-stress layer assumption and the approximation $Pr_m \approx Pr$, i.e. (2.8) and (2.9), further limit the model's utility to the inner layer and the near-wall region, respectively. It is noteworthy that (2.7) preserves the GRA relation's efficacy across varying Mach numbers (figure 3*a*) and Reynolds numbers (figure 3*b*), with their discrepancies from DNS data primarily attributed to the omission of higher-order terms in deriving (2.5) (see Appendix A for details).

In channel flows with asymmetric thermal boundary conditions, the total shear stress is given by $\bar{\tau}_t^+ = 1 - y/\delta_e$ for each wall side, when the flow is driven by a uniform body force. In this context, B_q, M_τ, $\tilde{u}^+$, y/δ_e, y^*, Pr are needed to derive $\tilde{T}/\tilde{T}_w$ via (2.7). As shown in figure 4, the GRA relation fails on both the cold lower and hot upper wall sides. In contrast, the proposed model is in close agreement with DNS data across various M_b, Re_b and $\tilde{T}_{w,H}/\tilde{T}_{w,L}$, especially in capturing the behaviour of $\mathrm{d}\tilde{T}/\mathrm{d}\tilde{u}|_e \to \infty$, which cannot be characterised by the quadratic relation provided in (1.1). Furthermore, the two associated approximations (2.8) and (2.9) continue to be applicable within their specific regions.

https://doi.org/10.1017/jfm.2025.10173 Published online by Cambridge University Press

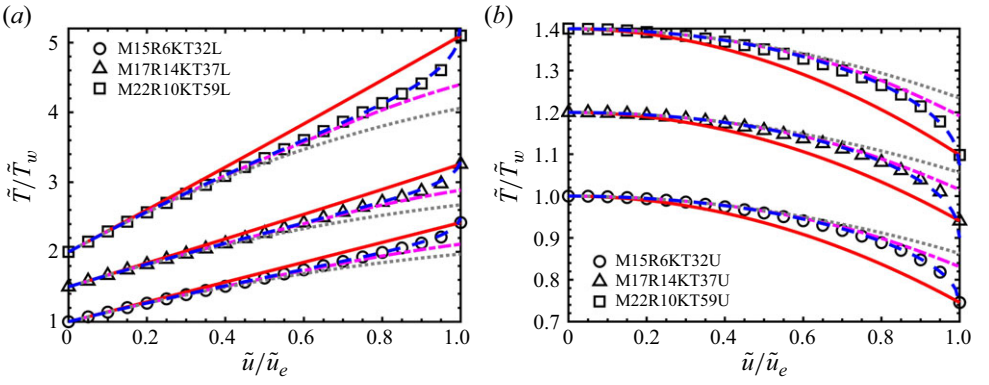


Figure 4. Comparison of DNS data for asymmetric cases (symbols) with various mean temperature–velocity relations. The equations corresponding to different line types are the same as those in figure 3. The datasets are sourced from Lusher & Coleman (2022) and Zhang *et al.* (2024). Plots in (*a*) and (*b*) show results within the boundary layers adjacent to the lower cold and upper hot walls, respectively, with upward shifts applied for clarity.

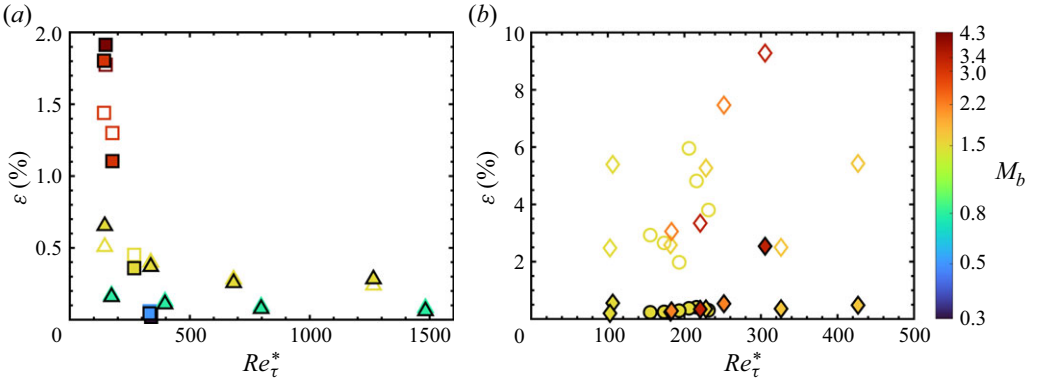


Figure 5. Integrated percentage errors of the mean temperature–velocity relations (1.1) (open symbols) and (2.7) (closed symbols) applied to (*a*) 14 profiles from symmetric cases, and (*b*) 16 profiles from asymmetric cases. The symbols □, △, ○ and ◇ represent DNS data from Zhang *et al.* (2023), Yao & Hussain (2020), Zhang *et al.* (2024), and Lusher & Coleman (2022), respectively.

For more quantitative assessments, the integrated percentage error is defined as

$$\varepsilon(\%) = \frac{\int_0^{\tilde{u}_e} \left| (\tilde{T}/\tilde{T}_w)_{pre} - (\tilde{T}/\tilde{T}_w)_{data} \right| \, \mathrm{d}(\tilde{u}/\tilde{u}_e)}{\int_0^{\tilde{u}_e} (\tilde{T}/\tilde{T}_w)_{data} \, \mathrm{d}(\tilde{u}/\tilde{u}_e)} \times 100\,\%, \tag{4.1}$$

where $(\tilde{T}/\tilde{T}_w)_{data}$ and $\tilde{u}/\tilde{u}_e$ are obtained from the DNS data, while $(\tilde{T}/\tilde{T}_w)_{pre}$ is predicted by the GRA relation and the proposed one, (1.1) and (2.7), respectively. The results are presented in figure 5. It can be clearly seen that the proposed model achieves accuracy that is nearly on a par with, or slightly inferior to, the GRA relation in symmetric cases, with all errors remaining below 2 %. Additionally, the present model shows a notable improvement when dealing with asymmetric thermal boundary conditions, with the majority of errors less than 1 %, in contrast to the GRA relation where all errors exceed 2 %. Notably, we also found that using either DNS data or the proposed model

https://doi.org/10.1017/jfm.2025.10173 Published online by Cambridge University Press

to determine Pr_m does not significantly impact the mean temperature profiles (see Appendix A for details), thus indirectly confirming the effectiveness of (3.1). Furthermore, the results demonstrate that the integrated percentage error increases with the bulk Mach number at a fixed characteristic Reynolds number Re_τ^*. Since the proposed relation exhibits a trend consistent with the GRA relation, we attribute this to the degradation of the same approximations underlying their derivations. For instance, the neglected fluctuating component in the approximation of the molecular diffusion flux (i.e. $\overline{\mu\,\mathrm{d}\phi/\mathrm{d}y} \approx \bar{\mu}\,\mathrm{d}\tilde{\phi}/\mathrm{d}y$) becomes increasingly significant as compressibility effects intensify.

5. Further discussions and applications

5.1. *Mean temperature decomposition and the modified GRA relation*

Zhang *et al.* (2014) have demonstrated that the GRA relations $\tilde{H}_g - \tilde{H}_w = U_w\tilde{u}$ and $H_g'' + c_p\phi'' = U_w u''$ (where $H_g = c_pT + r_g u^2/2$ is the general recovery enthalpy, ϕ'' denotes the residual temperature fluctuations, and $U_w = c_p\,\partial\tilde{T}/\partial\tilde{u}|_w$) can be admitted as similarity solutions by substituting them into the mean momentum and energy equations. By following a similar procedure, it can be derived that

$$\frac{\mathrm{d}}{\mathrm{d}y}\left(\bar{\mu}\frac{\mathrm{d}\tilde{\chi}}{\mathrm{d}y}\right) = 0, \tag{5.1}$$

for CTCFs, where $\tilde{\chi} = \tilde{H}_g - \tilde{H}_w - U_w\tilde{u}$. Meanwhile, the boundary conditions are given by

$$\begin{cases} y = 0, & \tilde{\chi} = 0, \\ y = \delta_e, & \dfrac{\mathrm{d}\tilde{\chi}}{\mathrm{d}y} = c_p\dfrac{\mathrm{d}\tilde{T}}{\mathrm{d}y}\bigg|_e + \dfrac{\tilde{u}_e^2}{2}\dfrac{\mathrm{d}r_g}{\mathrm{d}y}\bigg|_e. \end{cases} \tag{5.2}$$

It should be noted that (1.1) is derived under the assumption that the effective turbulent Prandtl number is $Pr_e = 1$, which implies $\mathrm{d}r_g/\mathrm{d}y = 0$. For channels with symmetric isothermal walls, it is straightforward to conclude that (5.1) and (5.2) permit the GRA relation $\tilde{\chi} = 0$ as $\mathrm{d}\tilde{T}/\mathrm{d}y = 0$ at the channel centre. However, such a solution is denied for cases with asymmetric thermal boundary conditions due to non-zero total heat flux at the boundary layer edge, despite complying with the governing equation and wall boundary conditions. This is the intrinsic reason why (1.1) is highly effective in symmetric cases yet inadequate for asymmetric cases, as evidenced in § 4.

By analysing (2.6*b*) and the results from § 4, it can be inferred that the GRA relation effectively describes the mean temperature component arising from turbulence production and viscous dissipation, but fails to account for the portion induced by $Q_{t,e} \neq 0$. To address this issue, we introduce a decomposition of the mean temperature into its 'pure' and 'residual' components, $\tilde{T} = \tilde{T}_{pure} + \tilde{T}_{res}$, where $\tilde{T}_{pure}$ is expected to be characterised by the GRA relation, and $\tilde{T}_{res}$ accounts for the physics of asymmetry. By introducing $\theta_{pure} = 1 - \tilde{T}_{pure}/\tilde{T}_w$ and $\theta_{res} = -\tilde{T}_{res}/\tilde{T}_w = \theta - \theta_{pure}$, (2.6*b*) can be separated into

$$\frac{\bar{\tau}_t^+}{Pr_m}\frac{\mathrm{d}\theta_{pure}}{\mathrm{d}\tilde{u}^+} = -(\gamma-1)\,M_\tau^2\int_{\tilde{u}^+}^{\tilde{u}_e^+}\bar{\tau}_t^+\,\mathrm{d}\tilde{u}^+, \quad \theta_{pure}\big|_w = 0, \tag{5.3}$$

and

$$\frac{\bar{\tau}_t^+}{Pr_m}\frac{\mathrm{d}\theta_{res}}{\mathrm{d}\tilde{u}^+} = Q_{t,e}, \quad \theta_{res}|_w = 0. \tag{5.4}$$

https://doi.org/10.1017/jfm.2025.10173 Published online by Cambridge University Press

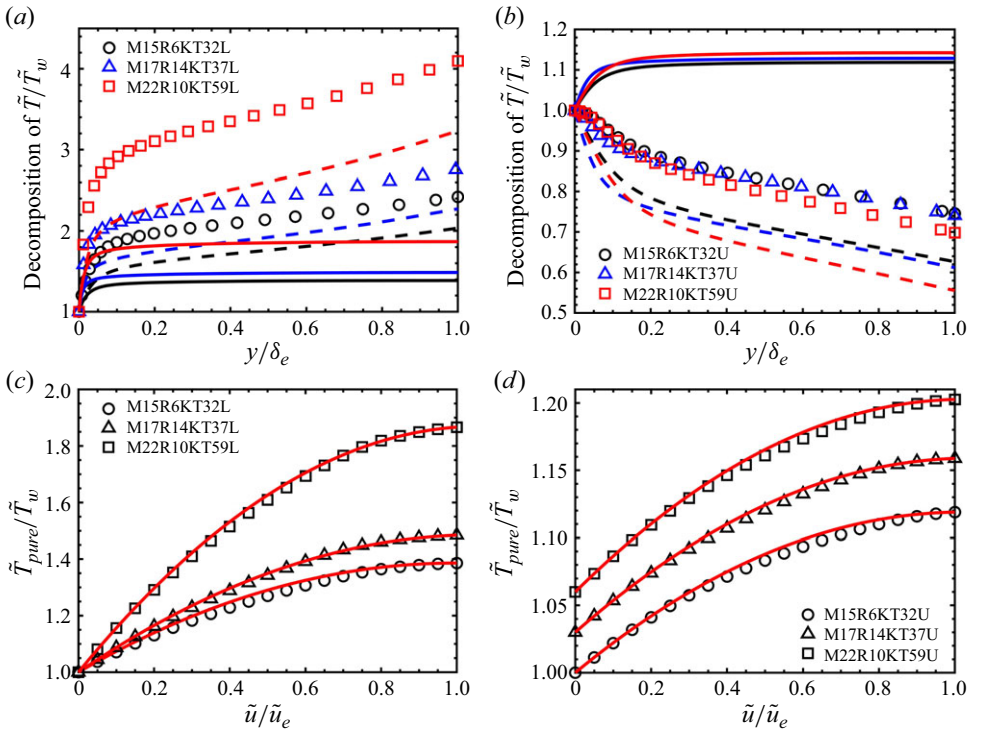


Figure 6. (*a,b*) Wall-normal distributions of the mean temperature ratio $\tilde{T}/\tilde{T}_w$ (symbols), along with the two components $\tilde{T}_{pure}/\tilde{T}_w$ (solid lines) and $\tilde{T}_{res}/\tilde{T}_w + 1$ (dashed lines). (*c,d*) Comparison of DNS data for $\tilde{T}_{pure}/\tilde{T}_w$ (symbols) with the modified GRA relation (5.1) (red solid lines). The data are from Lusher & Coleman (2022) and Zhang *et al.* (2024). Plots in (*a,c*) and (*b,d*) show results within the flow regions adjacent to the lower cold and upper hot walls, respectively, with upward shifts applied in (*c,d*) for clarity.

By replacing the mean temperature $\tilde{T}$ with its 'pure' component $\tilde{T}_{pure}$, it can be demonstrated that the modified GRA relation, $\tilde{H}_{g,m} - \tilde{H}_w = U_{w,m}\tilde{u}$ and $H''_{g,m} + c_p\phi'' = U_{w,m}u''$, is compatible with both the mean momentum and energy equations, as well as the associated boundary conditions. Therefore, the modified version of (1.1) can be expressed as

$$\frac{\tilde{T}_{pure}}{\tilde{T}_w} = 1 + \frac{\tilde{T}_{rg,m} - \tilde{T}_w}{\tilde{T}_w}\frac{\tilde{u}}{\tilde{u}_e} + \frac{\tilde{T}_{pure,e} - \tilde{T}_{rg,m}}{\tilde{T}_w}\left(\frac{\tilde{u}}{\tilde{u}_e}\right)^2, \tag{5.5}$$

where $\tilde{T}_{rg,m} = \tilde{T}_{pure,e} + r_{g,m}\tilde{u}_e^2/(2c_p)$ and $r_{g,m} = 2c_p(\tilde{T}_w - \tilde{T}_{pure,e})/\tilde{u}_e^2 + 2c_p/\tilde{u}_e \times \mathrm{d}\tilde{T}_{pure}/\mathrm{d}\tilde{u}|_w$.

Figure 6(*a,b*) present the results of the proposed mean temperature decomposition, where $1 + \tilde{T}_{res}/\tilde{T}_w$ is computed directly from DNS data and (5.4), while $\tilde{T}_{pure}/\tilde{T}_w$ is obtained by subtracting $\tilde{T}_{res}/\tilde{T}_w$ from $\tilde{T}/\tilde{T}_w$. As expected, the 'pure' component exhibits trends similar to those observed in symmetric cases, with a steep gradient near the wall that levels off in the bulk region. Meanwhile, the 'residual' component represents the additional mean temperature distribution induced by a constant total heat flux within the boundary layer, $\bar{q}_{t,res} = -(\bar{\lambda} + \bar{\lambda}_t)\,\mathrm{d}\tilde{T}_{res}/\mathrm{d}y = \bar{q}_{t,e}$, which is the intrinsic reason for

https://doi.org/10.1017/jfm.2025.10173 Published online by Cambridge University Press

the nearly linear profile of $\tilde{T}$ in the bulk region, as reported by Zhang *et al.* (2024). These findings provide valuable insights into the effects of asymmetric wall temperature. Moreover, the validity of (5.5) is demonstrated in figure 6(*c*,*d*), which is essentially equivalent to that in symmetric cases.

5.2. *Mean temperature transformations*

In this subsection, we briefly discuss another application of the total heat flux equation (2.6) for deriving mean temperature transformations, akin to using the total shear stress equation to derive mean velocity transformations (Hasan *et al.* 2023; Zhu *et al.* 2024).

Based on (2.6*a*), the total heat flux equation for the compressible state is expressed as

$$\frac{\bar{\tau}^+_{t,com}}{Pr_{m,com}}\frac{\mathrm{d}\theta}{\mathrm{d}\tilde{u}^+} = B_q + (\gamma-1)\,M_\tau^2\int_0^{\tilde{u}^+}\bar{\tau}^+_{t,com}\,\mathrm{d}\tilde{u}^+, \tag{5.6}$$

where the subscripts com and in denote compressible and 'incompressible' states, respectively. The 'incompressible' counterpart can be obtained by taking the limit $M_\tau \to 0$:

$$\frac{\bar{\tau}^+_{t,in}}{Pr_{m,in}}\frac{\mathrm{d}\bar{\mathcal{T}}^+}{\mathrm{d}\bar{U}^+} = \bar{q}^+_{t,in}, \tag{5.7}$$

where $\bar{U}^+$ and $\bar{\mathcal{T}}^+ = (\bar{\mathcal{T}}_w - \bar{\mathcal{T}})/\bar{\mathcal{T}}_\tau$ represent the inner-scaled mean velocity and temperature, respectively, adhering to the incompressible 'law of the wall'. Dividing (5.7) by (5.6), the general form of the mean temperature transformation is derived as

$$\bar{\mathcal{T}}^+ = \int_0^\theta \frac{Pr_{m,in}}{Pr_{m,com}}\frac{\bar{\tau}^+_{t,com}}{\bar{\tau}^+_{t,in}}\frac{\bar{q}^+_{t,in}}{B_q + (\gamma-1)\,M_\tau^2\int_0^{\tilde{u}^+}\bar{\tau}^+_{t,com}\,\mathrm{d}\tilde{u}^+}\frac{\mathrm{d}\bar{U}^+}{\mathrm{d}\tilde{u}^+}\,\mathrm{d}\theta, \tag{5.8}$$

where the kernel $\mathrm{d}\bar{U}^+/\mathrm{d}\tilde{u}^+$ can be combined with various velocity transformations. For example, under the constant-stress layer assumption $\bar{\tau}^+_{t,com} \approx \bar{\tau}^+_{t,in} \approx 1$, the Mach invariant assumption $Pr_{m,com}(Y^+) = Pr_{m,in}(Y^+)$, and the constant heat flux assumption for the 'incompressible' state $\bar{q}^+_{t,in} \approx 1$, the previously proposed VD-type and TL-type transformations for mean temperature can be derived by substituting the corresponding velocity kernels while setting $Y^+ = y^+$ and $Y^+ = y^*$, respectively. Detailed evaluations of these two transformations can be found in related studies (Chen *et al.* 2022*a*; Huang *et al.* 2023; Cheng & Fu 2024*a*).

6. Conclusions

The primary objective of this paper is to provide a unified framework for the analysis of mean temperature in CTCFs. Initially, a mean temperature–velocity relation and its two approximations, (2.7)–(2.9), are derived directly from the mean momentum and energy equations without invoking the presumed similarity or Reynolds analogies, complemented by an appropriate Pr_m model (3.1). A systematic and quantitative comparison with the DNS data reveals that the proposed relation performs comparably to the GRA relation (1.1) in symmetric channels, and maintains high efficacy in thermodynamically asymmetric cases, where the latter fails. Despite its complexity, our relation is more general and does not require edge-specific parameters such as $\tilde{u}_e$ and $\tilde{T}_e$, which are often difficult to determine (Cheng & Fu 2024*a*; Chen *et al.* 2025). The two approximations further demonstrate their accuracy within specific regions, highlighting the importance of comprehensive $\bar{\tau}_t^+$ information and proper Pr_m modelling for consistency across the

https://doi.org/10.1017/jfm.2025.10173 Published online by Cambridge University Press

entire boundary layer. Consequently, these relations have the potential to replace the GRA relation in predicting mean profiles of CTCFs, whether in modular iterative methods (Song, Zhang & Xia 2023) or in the algebraic near-wall models of Reynolds-averaged Navier–Stokes (Chen, Gan & Fu 2024) and wall-modelled large-eddy simulations (Chen *et al.* 2022*b*; Griffin, Fu & Moin 2023) approaches.

Additionally, we elucidate the intrinsic limitation of the GRA relation in asymmetric cases, where the non-zero mean temperature gradient at the boundary layer edge prevents it from being a similarity solution. By decomposing the mean temperature as $\tilde{T} = \tilde{T}_{pure} + \tilde{T}_{res}$, we show that the GRA relation captures only the 'pure' component associated with turbulence production and viscous dissipation, failing to account for the 'residual' part arising from the non-zero edge total heat flux $\bar{q}_{t,e}$. To address this issue, we derive and validate a revised formulation (5.5), which bridges the GRA relation to the proposed model. These findings highlight the need to reassess the GRA relation's applicability, particularly its compatibility with boundary conditions, which has been overlooked in previous studies.

Furthermore, the current framework enables the rigorous and intuitive derivation of mean temperature transformations corresponding to various velocity transformations, based on the compressible and 'incompressible' total heat flux equations. The combinations with more advanced velocity scalings such as the GFM (Griffin *et al.* 2021), HLPP (Hasan *et al.* 2023), and ZSYX (Zhu *et al.* 2024) transformations can be readily achieved, paving the way for developing more precise and robust temperature scalings. These scalings will motivate the extension of the incompressible eddy thermal conductivity $\bar{\lambda}_t/\bar{\lambda}$ to compressible flows, building upon the similar approach of Hendrickson *et al.* (2022, 2023) and Chen *et al.* (2024), and may further improve the near-wall model for mean temperature proposed by Chen *et al.* (2025). Additionally, the framework for predicting mean profiles in variable-properties forced air convection (Modesti & Pirozzoli 2024) may also be extended to high-speed flows. However, detailed investigations and evaluations are beyond the scope of this paper and will be reported in the near future.

Funding. This work was supported by the National Natural Science Foundation of China (NSFC grant nos 92152101 and 92152301). We extend our gratitude to J. Yao and F. Hussain, and D.J. Lusher and G.N. Coleman, for granting access to their direct numerical simulations data.

Declaration of interests. The authors report no conflict of interest.

Appendix A. Impact of approximations and simplifications on model accuracy

The original forms of (2.3) and (2.4) can be derived from the Reynolds-averaged momentum and total energy equations in (2.1) as

$$\bar{\mu}\frac{\mathrm{d}\tilde{u}}{\mathrm{d}y} + \bar{\mu}\frac{\mathrm{d}\overline{u''}}{\mathrm{d}y} + \overline{\mu'\frac{\mathrm{d}\mu'}{\mathrm{d}y}} - \bar{\rho}\,\widetilde{u''v''} = \bar{\tau}_w - \int_0^y \bar{F}\,\mathrm{d}y = \bar{\tau}_t, \tag{A1}$$

$$\overline{\tau_{i2}u_i} - \overline{\rho\tilde{u}_i u_i'' v''} - \frac{1}{2}\overline{\rho u_i'' u_i'' v''} + \bar{\lambda}\frac{\mathrm{d}\tilde{T}}{\mathrm{d}y} + \bar{\lambda}\frac{\mathrm{d}\overline{T''}}{\mathrm{d}y} + \overline{\lambda'\frac{\mathrm{d}T'}{\mathrm{d}y}} - c_p\bar{\rho}\,\widetilde{T''v''} = -\bar{q}_w - \int_0^y \bar{F}\bar{u}\mathrm{d}y, \tag{A2}$$

where no approximations or simplifications are introduced. Following an approach similar to that in § 2, the modified form of (2.6) can also be derived, from which $\theta = 1 - \tilde{T}/\tilde{T}_w$ can be further obtained via integration.

https://doi.org/10.1017/jfm.2025.10173 Published online by Cambridge University Press

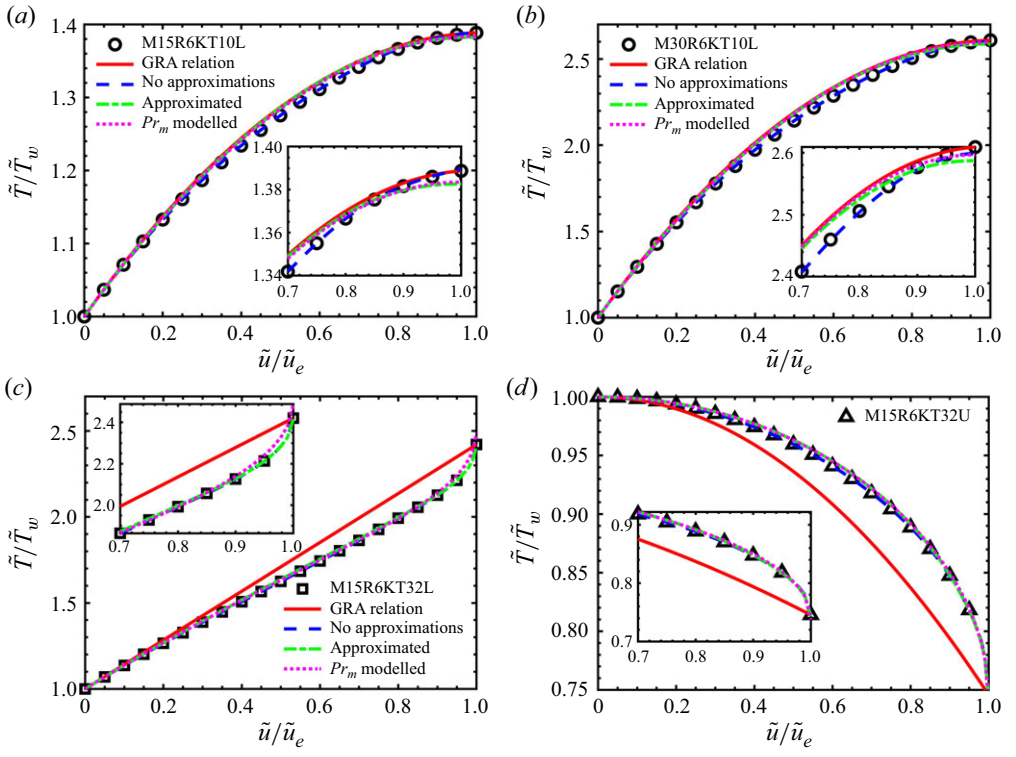


Figure 7. Comparison of DNS data (symbols) for (*a*,*b*) symmetric and (*c*,*d*) asymmetric cases with the GRA relation (red solid lines) and different versions of the proposed mean temperature–velocity relations. The blue dashed lines correspond to the integral relation that retains all higher-order terms neglected in (2.7), following (A1) and (A2), while computing Pr_m directly from DNS data. The green dash-dotted lines represent results obtained by neglecting higher-order terms as per (2.7) while still using Pr_m from DNS data, whereas the pink dotted lines show results obtained by further modelling Pr_m according to (3.1).

To preserve the simplicity of turbulence modelling and facilitate the derivation, the following approximations are adopted in the main text.

(i) The term $\overline{\tau_{i2}u_i}$ is approximated as (Huang *et al.* 1995, 2023)

$$\overline{\tau_{i2}u_i} = \mu\overline{\frac{\mathrm{d}K}{\mathrm{d}y}} + \mu\overline{\frac{\mathrm{d}k}{\mathrm{d}y}}, \tag{A3}$$

where $K = \tilde{K} + K''$ and $k = \tilde{k} + k''$ are defined in § 2.

(ii) The molecular diffusion flux of a quantity ϕ, $\overline{\mu\,\mathrm{d}\phi/\mathrm{d}y}$, is approximated by its dominant term $\bar{\mu}\,\mathrm{d}\tilde{\phi}/\mathrm{d}y$. Consequently, the mean momentum equation indicates that $\bar{\tau}_t^+ \approx \bar{\mu}^+\,\mathrm{d}\tilde{u}^+/\mathrm{d}y^+ - \overline{\rho u''v''}^+$. The term $\overline{\tau_{i2}u_i}$ is further simplified as $\overline{\tau_{i2}u_i} \approx \bar{\mu}\,\mathrm{d}\tilde{K}/\mathrm{d}y + \bar{\mu}\,\mathrm{d}\tilde{k}/\mathrm{d}y$, while the term $\bar{\lambda}\,\mathrm{d}\overline{T''}/\mathrm{d}y + \overline{\lambda'\,\mathrm{d}T'/\mathrm{d}y}$ is neglected.

(iii) The quasi-parallel flow approximation $u_iu_i \approx u^2$ and small turbulence approximation $u^2 \approx \tilde{u}^2 + 2\tilde{u}u''$ are further employed. Consequently, $\overline{\tau_{i2}u_i} \approx \bar{\mu}\,\mathrm{d}\tilde{K}/\mathrm{d}y \approx \tilde{u}\bar{\mu}\,\mathrm{d}\tilde{u}/\mathrm{d}y$ and $\overline{\rho\tilde{u}_iu_i''v''} \approx \bar{\rho}\tilde{u}\,\widetilde{u''v''}$. Additionally, the term $-1/2\overline{\rho u_i''u_i''v''}$ is neglected.

Figure 7 compares various mean temperature–velocity relations with DNS data (symbols). The red solid lines represent the GRA relation, while the blue dashed lines

https://doi.org/10.1017/jfm.2025.10173 Published online by Cambridge University Press

correspond to the results retaining all higher-order terms and using Pr_m computed from DNS data. The green dash-dotted lines represent the results from (2.7), with Pr_m also computed from DNS data. Obviously, the only difference between the blue dashed lines and the green dash-dotted lines lies in the above-mentioned approximations introduced in the derivation. First, the mean temperature profiles obtained from (A1) and (A2) perfectly match the DNS data, with only a minimal deviation where $\tilde{u}/\tilde{u}_e \to 1$, which may be attributed to errors introduced during the differentiation and integration. This result is not surprising, as the derivation is rigorous and all higher-order terms are retained. For cases with symmetric isothermal walls, figure 7(*a,b*) show that the above approximations visibly overestimate the mean temperature in most regions while slightly underestimating it where $\tilde{u}/\tilde{u}_e \to 1$. A more detailed comparison and analysis indicates that the former results primarily from the omission of fluctuating components in the molecular diffusion of mean kinetic energy and molecular heat flux, $\overline{\mu\,\mathrm{d}K/\mathrm{d}y}$ and $\overline{\lambda\,\mathrm{d}T/\mathrm{d}y}$, while the latter arises from neglecting the turbulent diffusion of turbulent kinetic energy, $-1/2\overline{\rho u_i'' u_i'' v''}$, and the approximation $\bar{\tau}_t^+ \approx \bar{\mu}^+\,\mathrm{d}\tilde{u}^+/\mathrm{d}y^+ - \overline{\rho u'' v''}^+$. A similar trend is also observed in asymmetric cases, where the deviations are minimal on the isothermal cold wall side, as shown in figure 7(*c,d*). The quasi-streamwise approximation $u_i u_i \approx u^2$ and the assumption $\overline{\tau_{i2} u_i} \approx \overline{\mu\,\mathrm{d}K/\mathrm{d}y} + \overline{\mu\,\mathrm{d}k/\mathrm{d}y}$ have negligible effects on model accuracy. It is worth noting that the implications of neglecting these higher-order terms are rather complicated, and their physical interpretation remains unclear. While we acknowledge the importance of a systematic and comprehensive analysis across various flow scenarios, such an investigation lies beyond the scope of the present study and is left for future work.

Additionally, we display mean temperature profiles predicted by (2.7) combined with the proposed Pr_m model (3.1), for comparison. These results are depicted by the pink dotted lines in figure 7. Obviously, the only difference between the green dash-dotted lines and the pink dotted lines lies in whether Pr_m is obtained directly from DNS data or modelled using the proposed approach. As observed, the proposed Pr_m model leads to an overestimation of the mean temperature when $\tilde{u}/\tilde{u}_e \to 1$, as we approximate $Pr_m = 1$ there for simplicity. However, this deviation is minor and localised, further demonstrating that the proposed Pr_m model effectively balances simplicity and accuracy.

In summary, neglecting higher-order terms in the derivation has a non-negligible impact on model accuracy. Unfortunately, these terms have yet to be effectively modelled, which is why previous studies have adopted approximations similar to ours (Huang *et al.* 1993, 1994, 2023; Huang & Coleman 1994; Gatski & Bonnet 2013; Zhang *et al.* 2014; Chen *et al.* 2022*a*; Cheng & Fu 2024*a*). Nonetheless, the above approximations remain a practical and concise approach for turbulence modelling. Future research is expected to systematically examine their effects and elucidate the underlying physical mechanisms, thereby helping to address current limitations and further enhance the proposed model.

References

Abe, H. & Antonia, R.A. 2019 Mean temperature calculations in a turbulent channel flow for air and mercury. *Intl J. Heat Mass Transfer* **132**, 1152–1165.

Busemann, A. 1931 *Handbuch der Experimentalphysik*, vol. 4. Geest und Portig.

Chen, P.E.S., Huang, G.P., Shi, Y.P., Yang, X.I.A. & Lv, Y. 2022*a* A unified temperature transformation for high-Mach-number flows above adiabatic and isothermal walls. *J.Fluid Mech.* **951**, A38.

Chen, P.E.S., Lv, Y., Xu, H.H.H.A., Shi, Y.P. & Yang, X.I.A. 2022*b* LES wall modeling for heat transfer at high speeds. *Phys. Rev. Fluids* **7** (1), 014608.

Chen, X.L., Gan, J.P. & Fu, L. 2024 An improved Baldwin–Lomax algebraic wall model for high-speed canonical turbulent boundary layers using established scalings. *J.Fluid Mech.* **987**, A7.

https://doi.org/10.1017/jfm.2025.10173 Published online by Cambridge University Press

CHEN, X.L., GAN, J.P. & FU, L. 2025 The mean temperature–velocity relation and a new temperature wall model for compressible laminar and turbulent flows. *J.Fluid Mech.* **1009**, A39.
CHENG, C., CHEN, X.L., ZHU, W.K., SHYY, W. & FU, L. 2024 Progress in physical modeling of compressible wall-bounded turbulent flows. *Acta Mech. Sin.* **40** (1), 323663.
CHENG, C. & FU, L. 2024*a* Mean temperature scalings in compressible wall turbulence. *Phys. Rev. Fluids* **9** (5), 054610.
CHENG, C. & FU, L. 2024*b* A Reynolds analogy model for compressible wall turbulence. *J.Fluid Mech.* **999**, A20.
CROCCO, L. 1932 Sulla trasmissione del calore da una lamina piana a un fluido scorrente ad alta velocita. *L'Aerotecnica* **12**, 181–197.
DUAN, L. & MARTIN, M.P. 2011 Direct numerical simulation of hypersonic turbulent boundary layers. Part 4. Effect of high enthalpy. *J.Fluid Mech.* **684**, 25–59.
GATSKI, T.B. & BONNET, J.-P. 2013 *Compressibility, Turbulence and High Speed Flow*. Academic Press.
GRIFFIN, K.P., FU, L. & MOIN, P. 2021 Velocity transformation for compressible wall-bounded turbulent flows with and without heat transfer. *Proc. Natl Acad. Sci. USA* **118** (34), e2111144118.
GRIFFIN, K.P., FU, L. & MOIN, P. 2023 Near-wall model for compressible turbulent boundary layers based on an inverse velocity transformation. *J. Fluid Mech.* **970**, A36.
HASAN, A.M., LARSSON, J., PIROZZOLI, S. & PECNIK, R. 2023 Incorporating intrinsic compressibility effects in velocity transformations for wall-bounded turbulent flows. *Phys. Rev. Fluids* **8** (11), L112601.
HENDRICKSON, T.R., SUBBAREDDY, P. & CANDLER, G.V. 2022 Improving eddy viscosity based turbulence models for high speed, cold wall flows. In AIAA SCITECH. 2022 Forum. AIAA.
HENDRICKSON, T.R., SUBBAREDDY, P., CANDLER, G.V. & MACDONALD, R.L. 2023 Applying compressible transformations to wall modeled LES of cold wall flat plate boundary layers, AIAA SCITECH. 2023 Forum.. AIAA.
HUANG, P.G., BRADSHAW, P. & COAKLEY, T.J. 1993 Skin friction and velocity profile family for compressible turbulentboundary layers. *AIAA J.* **31** (9), 1600–1604.
HUANG, P.G., BRADSHAW, P. & COAKLEY, T.J. 1994 Turbulence models for compressible boundary layers. *AIAA J.* **32** (4), 735–740.
HUANG, P.G. & COLEMAN, G.N. 1994 Van Driest transformation and compressible wall-bounded flows. *AIAA J.* **32** (10), 2110–2113.
HUANG, P.G., COLEMAN, G.N. & BRADSHAW, P. 1995 Compressible turbulent channel flows: DNS results and modelling. *J. Fluid Mech.* **305**, 185–218.
HUANG, P.G., COLEMAN, G.N., SPALART, P.R. & YANG, X.I.A. 2023 Velocity and temperature scalings leading to compressible laws of the wall. *J. Fluid Mech.* **977**, A49.
LLUESMA-RODRÍGUEZ, F., HOYAS, S. & PEREZ-QUILES, M.J. 2018 Influence of the computational domain on DNS of turbulent heat transfer up to $Re_\tau = 2000$ for $Pr = 0.71$. *Intl J. Heat Mass Transfer* **122**, 983–992.
LUSHER, D.J. & COLEMAN, G.N. 2022 Numerical study of compressible wall-bounded turbulence – the effect of thermal wall conditions on the turbulent Prandtl number in the low-supersonic regime. *Intl J. Comput. Fluid Dyn.* **36** (9), 797–815.
MODESTI, D. & PIROZZOLI, S. 2024 Friction and heat transfer in forced air convection with variable physical properties. *J. Fluid Mech.* **1001**, A27.
PATEL, A., BOERSMA, B.J. & PECNIK, R. 2017 Scalar statistics in variable property turbulent channel flows. *Phys. Rev. Fluids* **2** (8), 084604.
SMITS, A.J. & DUSSAUGE, J.P. 2006 *Turbulent Shear Layers in Supersonic Flow*. Springer Science & Business Media.
SONG, Y.B., ZHANG, P. & XIA, Z.H. 2023 Predicting mean profiles in compressible turbulent channel and pipe flows. *Phys. Rev. Fluids* **8** (3), 034604.
TRETTEL, A. & LARSSON, J. 2016 Mean velocity scaling for compressible wall turbulence with heat transfer. *Phys. Fluids* **28** (2), 026102.
VAN DRIEST, E.R. 1951 Turbulent boundary layer in compressible fluids. *J. Aeronaut. Sci.* **18** (3), 145–160.
WALZ, A. 1969 *Boundary Layers of Flow and Temperature*. MIT Press.
YAO, J. & HUSSAIN, F. 2020 Turbulence statistics and coherent structures in compressible channel flow. *Phys. Rev. Fluids* **5** (8), 084603.
YU, M., DONG, S.W., YUAN, X.X. & XU, C.X. 2024 Statistics and dynamics of coherent structures in compressible wall-bounded turbulence. *Sci. China Phys. Mech. Astron.* **67** (12), 124701.
ZHANG, P., SONG, Y.B. & XIA, Z.H. 2023 Compressibility effect in compressible turbulent channel flows (in Chinese). *Sci. Sin. Phys. Mech. Astron.* **53** (4), 244711.
ZHANG, P., SONG, Y.B. & XIA, Z.H. 2024 Direct numerical simulations of compressible turbulent channel flows with asymmetric thermal walls. *J. Fluid Mech.* **984**, A37.

https://doi.org/10.1017/jfm.2025.10173 Published online by Cambridge University Press

ZHANG, P. & XIA, Z.H. 2020 Contribution of viscous stress work to wall heat flux in compressible turbulent channel flows. *Phys. Rev. E* **102** (4), 043107.

ZHANG, Y.S., BI, W.T., HUSSAIN, F. & SHE, Z.S. 2014 A generalized Reynolds analogy for compressible wall-bounded turbulent flows. *J. Fluid Mech.* **739**, 392–420.

ZHU, X.K., SONG, Y.B., YANG, X.S. & XIA, Z.H. 2024 Velocity transformation for compressible wall-bounded turbulence – an approach through the mixing length hypothesis. *Sci. China Phys. Mech. Astron.* **67** (9), 294711.

https://doi.org/10.1017/jfm.2025.10173 Published online by Cambridge University Press